# Facile fabrication of rGO/PPy/nZVI catalytic microreactor for ultrafast removal of p-nitrophenol from water

Yanyan Chen [a,1], Manlin Zhang [a,1], Tiantian Chen [a], Ganbing Zhang [c], Hui Xu [a,*], Hongwei Sun [a,*], Lizhi Zhang [b]

[a] *Key Laboratory of Pesticide & Chemical Biology, Ministry of Education, College of Chemistry, Central China Normal University, Wuhan 430079, China*
[b] *School of Environmental Science and Engineering, Shanghai Jiao Tong University, Shanghai 200240, China*
[c] *College of Chemistry and Chemical Engineering, Hubei University, Wuhan 430062, China*

A R T I C L E   I N F O

A B S T R A C T

The application of powdered nanoscale zero-valent iron (nZVI) in conventional reactors for water treatment is limited by insufficient mass-transfer and difficult post-separation of catalysts. Herein, a novel microreactor was constructed by anchoring nZVI on the reduced graphene oxide/polypyrrole nanocomposite (rGO/PPy) substrate within the microchannel of a stainless-steel tube through two-step electrodeposition, which catalyzed the Fenton-like reaction to remove > 99% p-nitrophenol (PNP) within 50 s, outperforming traditional batch reactors. The rGO/PPy composite substrate consolidated the adhesion on steel surface, stabilized the nZVI by forming electron-transfer complex, facilitated the decomposition of $H_2O_2$ to free •OH, and promoted the redox cycle of Fe(III)/Fe (II) via the electron donating capacity of rGO/PPy. Besides, the significant convection and highly-effective mass transfer within the microreactor also contributed to the ultrafast PNP removal. With acceptable durability, easy re-generation, and scalability, the rGO/PPy/nZVI microreactor is promising for the ultrafast removal of pollutants from water.

## 1. Introduction

Among various catalysts and techniques developed for the environmental pollutants removal [1–4], nanoscale zero-valent iron (nZVI), as an effective Fenton-like catalyst, has been extensively employed for the decontamination of inorganic and organic pollutants because of its low reduction potential ($E^\theta$ = −0.44 V), large specific surface area, high activity and low toxicity [5,6]. Despite substantial progresses have been made in the fabrication and application of nZVI for the abatement of water contaminants such as metals, metalloids, nitrate, and organic pollutants [7,8], much fewer efforts were made in the design of nZVI-based reactors for water treatment. Most studies conducted the pollutant removal of nZVI with batch experiments in flasks, but would

be faced with problems during real water treatment scenario, e.g., the poor dispersibility of nZVI, the insufficient mass-transfer at the catalyst-solution interface, and the post-separation of nZVI after reaction. For instance, Li et al. employed a sequencing batch reactor of nZVI, which consisted of the nZVI slurry reaction, the nZVI post-separation, the nZVI recycle, and the aeration/coagulation/sedimentation modules [9]. Although this reactor could achieve effective heavy metal removal from wastewater, it was unable to operate in continuous-flow mode. The nZVI fixed bed reactors (e.g., by packing the mixture of nZVI and gravel in columns, or by vacuum filtrating nZVI on the supporting membranes) with the flow-through reaction mode could achieve continuous operation, but suffered from the easy clogging of columns or fouling of membranes, caused by the iron corrosion, iron oxides

production, volume expansion, and the gas evolution [10,11]. Compared with the flow-through mode of reaction, the flow-by mode reactors may help tackle the problems of column clogging and membrane fouling. However, conventional design of flow-by reactors required immobilizing highly dispersed catalysts on bulk substrates. By loading nZVI on graphene [12], activated carbon [13], mesoporous carbon [14], zeolite [15] and biochar [16], etc., the aggregation of nZVI could be alleviated [17], but the immobility of nZVI may limit the mass transfer efficiency between the nZVI and the contaminated solution, thus may restrain the performance. Therefore, it is still challenging to rationally design novel nZVI reactors to achieve the effective and continuous water purification.

Microreactors, a new type of continuous flow tubular reactor with the channel diameter in the range of 10–1000 μm, have recently attracted increasing interests in catalysis, synthesis of nanoparticle and fine chemicals [18]. The micro-channel configuration, continuous flow design, and highly dispersed catalysts give the microreactor excellent catalytic performance due to the intrinsically high mass and heat transfer efficiencies [19,20]. Other merits include no post-separation of catalysts, easy operation, improved safety, and up-scalability [21,22]. These advantages of microreactors may thus offer new opportunities to tackle the problems facing the nZVI water treatment. Besides, the susceptibility of nZVI to oxidation during fabrication and storage is also the main problem at present. By in-situ depositing the nZVI in the microchannels, the oxidation of nZVI shall be greatly suppressed thanks to the restrained diffusion of oxygen within the microchannels. Moreover, the confined space within the microchannels shall allow the close vicinity of the in-situ generated reactive species to target contaminants, avoiding the self-quenching of short-lived reactive species and facilitating the ultrafast removal of contaminants [23]. Therefore, we suppose that the design of microreactor may help boost the performance of nZVI and tackle the problems of conventional reactors. But unfortunately, such studies are not available till now, which drove us to explore the feasibility of the nZVI microreactor.

The loading of nZVI particles in the microchannels could be achieved by the in-situ electrodeposition of ferrous ions. However, our preliminary trial suggested that the direct electrodeposition of $Fe^{2+}$ on the inner surface of the stainless steel (SS) tube resulted in large aggregates of nZVI with poor reactivity. Therefore, a substrate layer on SS was necessary for the effective loading and dispersion of nZVI within the microchannels. Two-dimensional carbon materials such as graphene, graphene oxide (GO), and reduced graphene oxide (rGO) are characterized with high specific surface area, outstanding electron transport properties, and the favorable p-π interaction with metals, making them ideal supporting materials of nZVI [24–28]. Nevertheless, our previous trial proved that GO alone cannot be effectively electrodeposited on the SS surface. Therefore, the processability of GO needs to be improved for its firm adhesion on the surface of SS. Polypyrrole (PPy) is a conductive polymer with low cost and strong mechanical stability. PPy can be facilely fabricated by electrochemical polymerization of pyrrole monomers, during which GO sheets can be easily incorporated into the polymeric matrix and reduced to rGO, concurrently enhancing both the processability and conductivity of GO. Besides, rGO and PPy might form the donor-acceptor complex via electrostatic, π-π and p-π interactions, which may render the rGO/PPy membrane better chemical stability. Better adsorption of organic pollutants may also be achieved via the π-π stacking interactions between contaminants and the rGO/PPy composite [29], more importantly, rGO was reported to donate electrons during the Fenton-like reactions [30]. Therefore, we can expect synergistic effects between rGO/PPy and nZVI in the microreactor for pollutant removal.

Herein, we first constructed a PPy/rGO/nZVI nanocomposite based microreactor through a facile two-step electrodeposition method. The microreactor was used to catalyze the Fenton-like reaction for the removal of p-nitrophenol (PNP), which is highly toxic, recalcitrant to biodegradation, and poorly removed by traditional water treatment

techniques. Besides, PNP has been frequently used as the model pollutants of advanced oxidation techniques (AOT), thus facilitates the comparison of our work with other AOT. Excitingly, the PPy/rGO/nZVI microreactor rapidly removed PNP, outperforming conventional reactors. The reusability and regeneration of the microreactor were investigated, and the interfacial interactions of the rGO/PPy/nZVI nanocomposite were revealed by experimental and theoretical methods. The possible pathways of PNP degradation were also proposed. This work represents a novel and promising design of nZVI reactor for water purification.

## 2. Materials and methods

### 2.1. Chemicals

Graphene oxide (GO) was purchased from Xianfeng Nanomaterial Technology Co. Ltd. (Nanjing, China). Pyrrole (Py, 98%), sodium dodecyl sulfonate (SDS) (99%), ferrous sulfate heptahydrate ($FeSO_4 \bullet 7 H_2O$) (98%), hydrochloric acid (38%), sodium hydroxide (96%), sodium nitrate (99%), sodium sulfate (99%), disodium hydrogen phosphate (99%), isopropyl alcohol (99.7%) and chloroform (99%) were provided by Sinopharm Chemical Reagent Co. Ltd. (Shanghai, China). Hydrogen peroxide (30%, $H_2O_2$), p-nitrophenol (PNP, 98%) and 5,5-dimethyl-1-pyrroline N-oxide (DMPO) (97%) were obtained from Aladdin Industrial Corporation (Shanghai, China). HPLC-grade methanol (99.9%) was purchased from Thermo Fisher Technology (China) Co., Ltd. HPLC-grade acetonitrile was purchased from Merck Company (Germany) Inc. Ultrapure water used in the experiments was produced by the arium® pro-Ultrapure Water Systems (Sartorius Stedim Biotech, Gottingen, Germany).

### 2.2. Preparation of rGO/PPy/nZVI catalytic microreactor

The schematic diagram of preparation catalytic membrane is presented in Fig. S1a. In the first step (Fig. S1b), pyrrole monomers (0.24 mol $L^{-1}$) and SDS (0.08 mol $L^{-1}$) were added to 3.0 mL ultrasonically dispersed GO suspension and mixed thoroughly as electrolyte solution. Prior to electrodeposition, a SS tube was washed with ultrapure water and methanol. Then one end of the SS tube was connected to a syringe, and the other end was immersed in the electrolyte solution. 1.0 mL of the electrolyte solution was delivered through the SS tube by using a syringe pump at the flow rate of 0.2 mL $min^{-1}$. Simultaneously, with the SS tube and a SS wire as anode and cathode, electrodeposition was carried out at a constant potential of 7.5 V for 1 min [31]. Then the tube was washed with methanol and water to remove the residual electrolyte solution, and dried at 60 °C for 2 h.

In the second step (Fig. S1c), the rGO/PPy coated SS tube (cathode) and a SS wire (anode) were simultaneously immersed in the electrodeposition solution (0.60 mol $L^{-1}$ $FeSO_4 \cdot 7 H_2O$), and dynamical electrodeposition was conducted for 2 min under the same voltage and flow rate. Finally, the rGO/PPy/nZVI microreactor was obtained after the above-mentioned washing and drying procedure. The as-prepared microreactors were characterized by field emission scanning electron microscopy (FESEM), transmission electron microscope (TEM), X-ray diffraction (XRD), X-ray photoelectron spectroscopy (XPS), and atomic absorption spectrum (AAS), with the details given in the Text S1 of the supplementary materials.

### 2.3. PNP degradation experiments

Standard stock solution of 10 mg $L^{-1}$ PNP was prepared in ultrapure water, its pH was adjusted by 1.0 M HCl and 1.0 M NaOH solutions. 1.0 mL of the reaction solution was delivered through rGO/PPy/nZVI microreactor at the flow rate of 0.5 mL $min^{-1}$ with a syringe pump. The eluent solution was collected and isopropyl alcohol was added to quench •OH. After filtrating by a 0.22 μm nylon filter membrane, 20 μL of the

filtrate was analyzed by high performance liquid chromatography (HPLC, Text S2, supplementary materials) to quantify the remaining concentrations of PNP. The degradation intermediates of PNP were analyzed using a liquid chromatography-mass spectrometry system (LC-MS, Waters, Manchester, UK) as described in text S2 of the supplementary materials. All experiments were performed in triplicate and the average values are reported. The schematic diagram of degradation procedure is presented in Fig. S1d. The capture experiments of reactive species during the Fenton-like reactions were carried out with electron paramagnetic resonance (EPR, Bruker EMXmicro, Germany).

### 2.4. DFT calculation

Based on surface cluster model, the adsorption, degradation pathway of $H_2O_2$ on the surface of rGO/PPy/nZVI microreactor, the impact of PPy on the catalytic performance, and the charge transfer interaction between rGO/PPy and Fe (III) were studied by using density functional theory (DFT) method with the Gaussian 09 program. The rGO was modeled by a $C_{28}H_{14}$ cluster with the $C_{28}$ graphite flake and 14 hydrogen atoms saturating the edge carbon atoms. Trimeric pyrroles were used for modeling the PPy. All the clusters were optimized with the PBE functional. The effective core potential (ECP) SDD and the additional basis set were used for Fe, and 6–31 G (d, p) were adopted for non-metal atoms. Frequency analyses were performed to verify the optimized
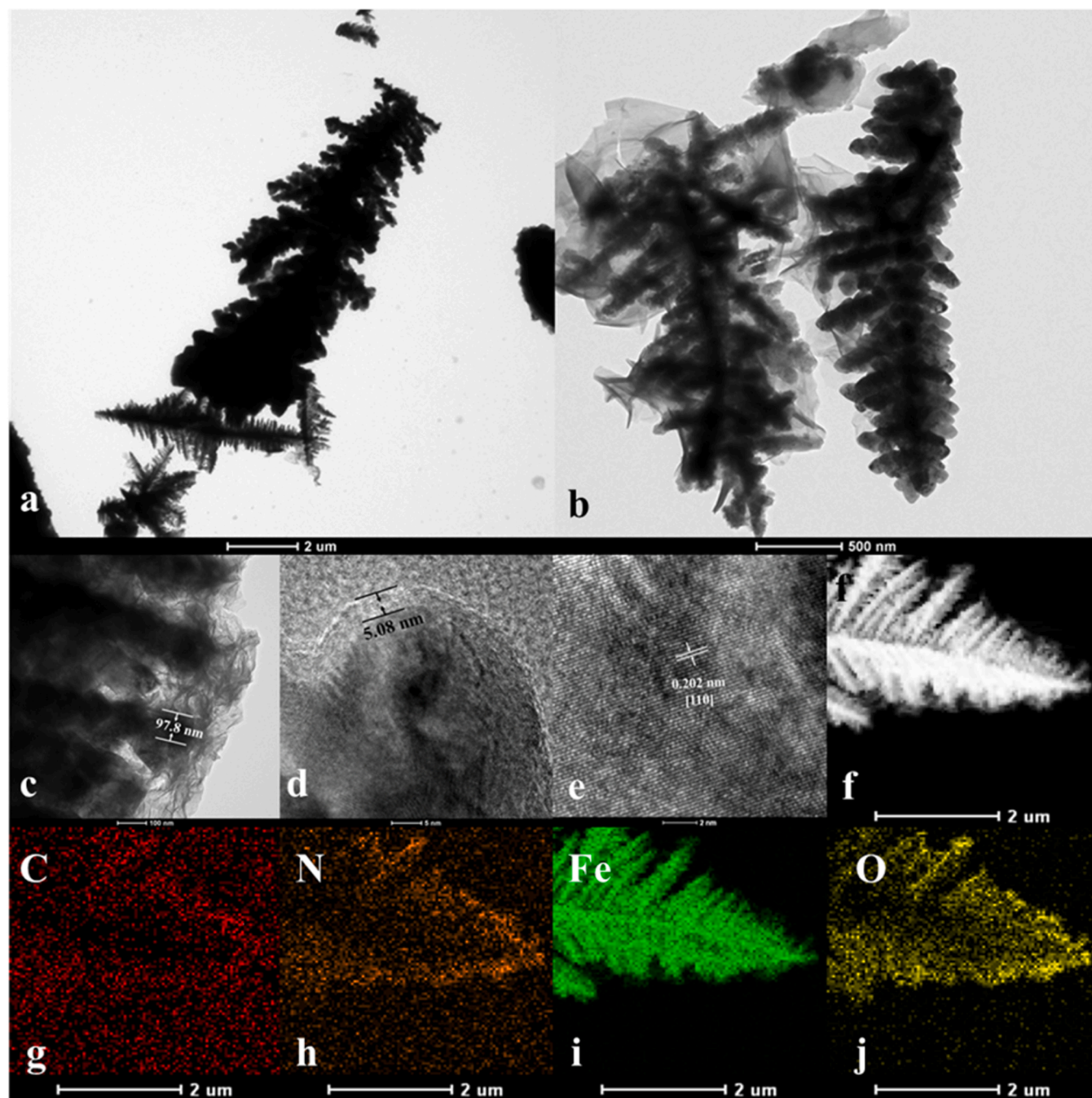


**Fig. 1.** TEM images of (a) nZVI, (b, c) rGO/PPy/nZVI. HR-TEM images of (d) rGO/PPy/nZVI, (e) the rGO/PPy/nZVI nanostructures. (f-j) The elemental mappings of the rGO/PPy/nZVI nanocomposite. Fabricating conditions: SS tube length 20 cm, id. 1 mm); electrodeposition time of rGO/PPy and nZVI: 60 s and 120 s; electrodeposition voltage: 7.5 V.

geometries regarding the energetic minima and to obtain thermodynamic functions such as enthalpy (H) and Gibbs free energy (G). Natural bond orbital (NBO) analyses were carried out to describe the orbital interactions between the subsections of the rGO/PPy/nZVI nanocomposites based on their optimized geometries. The adsorption enthalpy ($\Delta H_{ads}$) and Gibbs free energy ($\Delta G$) were defined as follows:

$$\Delta H_{ads} = H_{AB} - H_A - H_B \tag{1}$$

$$\Delta G = G_{AB} - G_A - G_B \tag{2}$$

where $H_{AB}$ is the thermal enthalpy of the optimized adsorbed structure of Fe atom over substrates (rGO/nZVI or rGO/PPy/nZVI), $H_A$ and $H_B$ are the thermal enthalpy of Fe atom and substrate (rGO or rGO/PPy), respectively. With the definition, more negative values reflect the stronger interaction and higher stability of the supported nZVI catalysts. The adsorption Gibbs free energy ($\Delta G$) was calculated according to Eq. (2) with similar definition as Eq. (1).

## 3. Results and discussion

### 3.1. Preparation of the rGO/PPy/nZVI microreactor

The structures of the nZVI, rGO/PPy and rGO/PPy/nZVI were characterized by SEM (Fig. S2), TEM and HRTEM (Fig. 1). The SEM image of rGO/PPy in Fig. S2a displayed that many clustered hemispherical particles of polypyrrole were embedded in the hierarchical and wrinkle-like nanosheets of rGO, indicating the successful fabrication of the rGO/PPy substrate, and the possible mechanism could be described as follows. Both the pyrrole monomers and GO will adsorb on the surface of the anode, where the pyrrole monomers would be oxidized to radical cations, with the electrons captured by GO to form rGO. The pyrrole radical would easily polymerize and attach to the adjacent rGO sheets, resulting in the formation of rGO/PPy nanocomposite. The anionic surfactant SDS was added during the fabrication procedure, to improve the dispersibility of GO and the solubility of pyrrole monomers, and to increase the electrical conductivity of PPy [32]. The resulting rGO/PPy nanocomposite possessed enhanced conductivity than GO, arisen from the π–π stacking between PPy backbone and the rGO sheets [33].

As shown in Figs. S2b and 1a, the electro-deposited nZVI particles (without rGO/PPy substrate) formed large dendritic structures of several micrometers, which may arise from the symmetric electric field within the annular cylinder SS tube and the gradient concentration of $Fe^{2+}$ near the SS surface, as described in a previous report [34]. When nZVI was electrodeposited on the rGO/PPy substrate (rGO/PPy/nZVI), the nZVI still maintained the dendritic structures (Fig. S2c and d), covered with wrinkled rGO/PPy sheets (Fig. 1b). The dendritic nZVI was the assembly of nanospheres of ca. 50–100 nm (Fig. 1c), which showed the typical oxidized shell of ca. 5 nm thickness (Fig. 1d), and the $Fe^0$ core with the interplanar distance of 0.202 nm in the HRTEM image, ascribing to the (110) plane of α-$Fe^0$ (Fig. 1e). Compared with the bare nZVI, rGO/PPy supported nZVI were characterized by smaller size and better dispersibility, which may increase the surface area and active sites for the catalytic Fenton-like reaction. The energy dispersive spectroscopy (EDS) images indicated the uniform distribution of C, N elements, representing the rGO/PPy substrate, whereas Fe and O elements existed in dendritic shape, corresponding to the nZVI (Fig. 1g-j). In the XRD patterns, the broad diffraction peak centered at 23.57° was ascribed to graphitized carbon [35], and the peaks at 44.71°, 65.18°, and 82.38° were indexed to the (110), (200), and (211) planes of α-$Fe^0$ (Fig. 2) [12,36]. All the results collectively proved that the successful fabrication of rGO/PPy/nZVI catalysts.

The chemical states of the elements in rGO/PPy/nZVI were further investigated by XPS (Fig. 3). Three peaks at 284.88, 286.53, and 288.82 eV in the C 1 s spectrum corresponded to the non-oxygen carbon (C-C/C=C), C-O and C=O groups, respectively [24,37–39]. C=C stemmed from the aromatic rings of rGO and the conjugated carbon
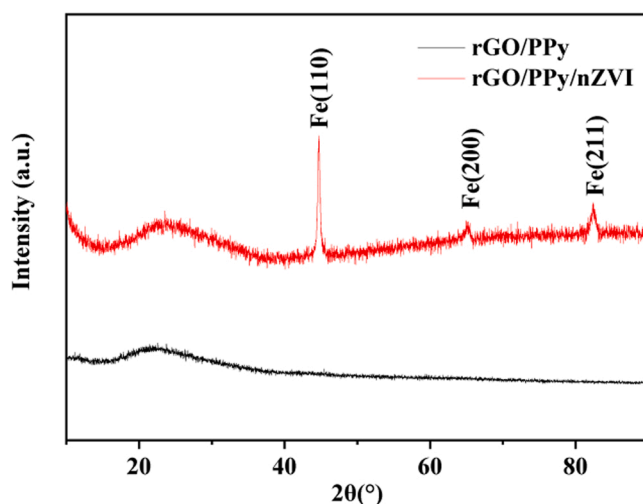


**Fig. 2.** XRD of rGO/PPy and rGO/PPy/nZVI nanocomposites.

atoms of PPy, whereas C-O and C=O signals indicated the incomplete reduction of GO during electrodeposition and the presence of oxygen-containing group residues such as hydroxyl and carboxyl groups. This was consistent with the results of EDS, which showed the distribution of O within the rGO substrate (Fig. 1j). The N 1 s spectrum was deconvoluted to three peaks at 397.67, 399.82, and 401.58 eV, which were attributed to pyridinic N, pyrrolic N and graphitic N, respectively. Pyrrolic N was dominant, corresponding to the N of PPy. The EDS mapping results also confirmed the abundant N species in the rGO/PPy/nZVI nanocomposite. The O 1 s spectrum were decomposed into three peaks located at 530.07, 531.74 and 533.39 eV, which were respectively attributed to oxide ($O^{2-}$), hydroxide (-OH) and attached water [40]. The dominant hydroxide (-OH) probably originated from the oxygen-containing groups of rGO and the surface -OH groups of nZVI. The oxide ($O^{2-}$) species referred to the lattice oxygen atoms in the shell of nZVI, as shown by the HRTEM image (Fig. 1d and e). Furthermore, the five characteristic peaks of Fe 2p spectrum can be assigned to $Fe^0$ (706.69 eV), satellite peak of Fe 2p (718.80 eV), Fe(II) (Fe $2p_{1/2}$: 710.89 eV), Fe(III) (Fe $2p_{3/2}$: 713.23 eV; Fe $2p_{1/2}$:724.98 eV), respectively [41–43]. The Fe(II) and Fe(III) peaks confirmed the presence of iron oxide/hydroxide shell that coated the $Fe^0$ core due to the in-situ oxidation of nZVI surface [42,44].

### 3.2. Fenton-like performance of the rGO/PPy/nZVI microreactor

The removal of PNP was used to evaluate the Fenton-like performance of rGO/PPy/nZVI microreactor, and the parameters of the microreactor fabrication were first optimized. The inner diameter and length of the microreactor may impact the loading amount of catalysts, thus influencing the catalytic performance of the rGO/PPy/nZVI microreactor. With the increase of SS tube inner diameter from 0.5 to 1.0 mm, the coating thickness of the rGO/PPy/nZVI membrane decreased from 16.35 to 7.7 μm, but the dendritic nanostructure of nZVI maintained (Fig. S3). However, the removal efficiencies of PNP were positively correlated with the inner diameter in the range of 0.5–1.0 mm (Fig. 4a). Smaller inner diameter of SS tube resulted in thicker rGO/PPy/nZVI membrane, but the active sites to catalyze the Fenton-like reaction were often on the surface of the membrane, those embedded in the bulk phase of membrane were not available for the reaction. Besides, too thick membrane shall cause its loose adhesion on the SS surface and possible peeling off during reaction. Smaller inner diameter will also result in the decreased water flux, increased back-pressure and higher cost. Therefore, inner diameter of 1.0 mm was employed in our following experiments. The impacts of the rGO/PPy/nZVI microreactor length was also investigated. As shown in Fig. 4b, when the length of the
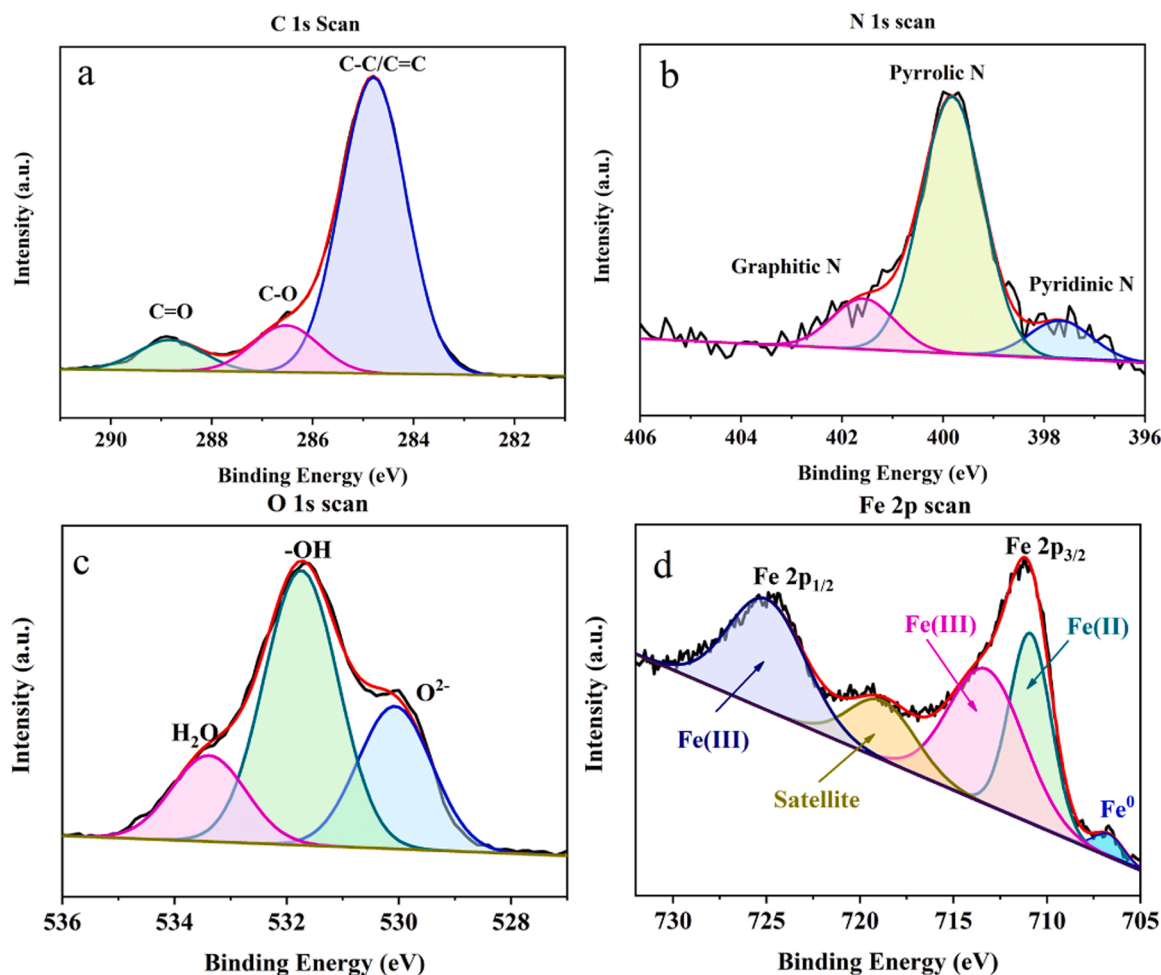
**Fig. 3.** XPS spectra of rGO/PPy/nZVI nanocomposites: (a) C 1 s peaks; (b) N 1 s peaks; (c) O 1 s peaks and (d) Fe 2p peaks.

tube increased from 5 to 60 cm at the identical inner diameter of 1.0 mm, the removal performance of PNP improved sharply from 67.1% (5 cm) to 94.4% (20 cm), and did not change significantly thereafter with the further increase of tube length to 60 cm (99.3%). The morphology of the rGO/PPy/nZVI membrane fabricated using different SS tube length was also characterized with the SEM (Fig. S4). The dendritic nanostructure of nZVI changed at different length. The nZVI at 20 cm showed clear secondary structures including the trunk, branches, and leaves, but the fine structures blurred at 5 and 10 cm due to the over-growth of nZVI crystals. On the contrary, nZVI fabricated with 40 and 60 cm tubes were sparser and more scattered. The possible cause is that longer SS tube raised the electrical resistance (15.6, 21.3, 31.1, 42.5 and 68.6 $\Omega$ for 5, 10, 20, 40, 60 cm tubes, respectively) and lowered the deposition current, responsible for the different deposition amount of nZVI. Obviously, the SS tube of 20 cm were the optimal length to prepare the microreactor. The impact of electrodeposition time were also investigated. The increase of rGO/PPy deposition time during step 1 from 30 to 60 s improved the PNP removal efficiencies from 80.1% to 94.9%, but further increasing deposition time to 120 s resulted in little improvement of PNP degradation (99.3%) (Fig. 4c). SEM images indicated that the thickness of the rGO/PPy substrate increased from 2 to 16.6 μm with the increased deposition time from 30 to 120 s (Fig. S5a-S5f). Besides, Longer deposition time of the rGO/PPy substrate may provide more binding sites for the nucleation and growth of nZVI, resulting in the better dispersion and smaller size of nZVI (Fig. S5g-S5i), which can provide more catalytic sites for the Fenton-like removal of PNP. Therefore, rGO/PPy electrodeposition time of 60 s was employed for the next experiments. The impact of nZVI electrodeposition time in

step 2 was also studied. PNP removal efficiency increased rapidly with longer deposition of nZVI in the range of 30–90 s, but increased less thereafter (Fig. 4c). SEM images showed that longer nZVI deposition time increased the thickness of the rGO/PPy/nZVI membrane from 4.85 to 14.45 μm, with rougher surface, smaller nZVI size, and clearer dendritic structures (Fig. S6), beneficial for catalytic reactions. However, too thick rGO/PPy/nZVI membrane would cause the poor mechanical strength and easy drop from the SS surface (Fig. S7). Therefore, 120 s was selected. Under these optimal conditions, ca. 5.5 mg rGO/PPy/nZVI membrane (thickness: about 7.7 μm) with 48.7% iron content was prepared (Fig. S8), achieving 94.9% PNP removal.

The operating conditions of the microreactor in the Fenton-like reaction were also optimized, including the $H_2O_2$ concentrations, the pH values, and the flow rate of influent. With the increase of $H_2O_2$ concentrations, the PNP removal efficiency first increased and then decreased, and the maximum removal of PNP was achieved at 6.52 mmol/L $H_2O_2$ (Fig. 4d). The results might be attributed to the following two reasons: (1) increased $H_2O_2$ concentration led to the generation of more •OH, which was conducive to the removal of PNP; (2) excessive $H_2O_2$ would compete •OH and suppress PNP removal [45]. Regarding the impact of solution pH, the PNP removal reached its maximum (94.9%) at pH 3 and decreased to ca. 90% at pH 2 and 4 (Fig. 4e), consistent with the characteristics of Fenton reactions [46]. The flow rate of influent determined the residence time ($\tau$) within the microreactor, and flow rates of 0.2, 0.3, 0.4, 0.5, and 0.6 mL min$^{-1}$ were investigated, corresponding to $\tau$ of 50, 33, 25, 20, and 17 s. Surprisingly, high removal ratio of PNP (99.6% at 0.2 mL min$^{-1}$) could maintain in the range of 0.2–0.5 mL min$^{-1}$, and decreased to ca. 80% at 0.6 mL min$^{-1}$
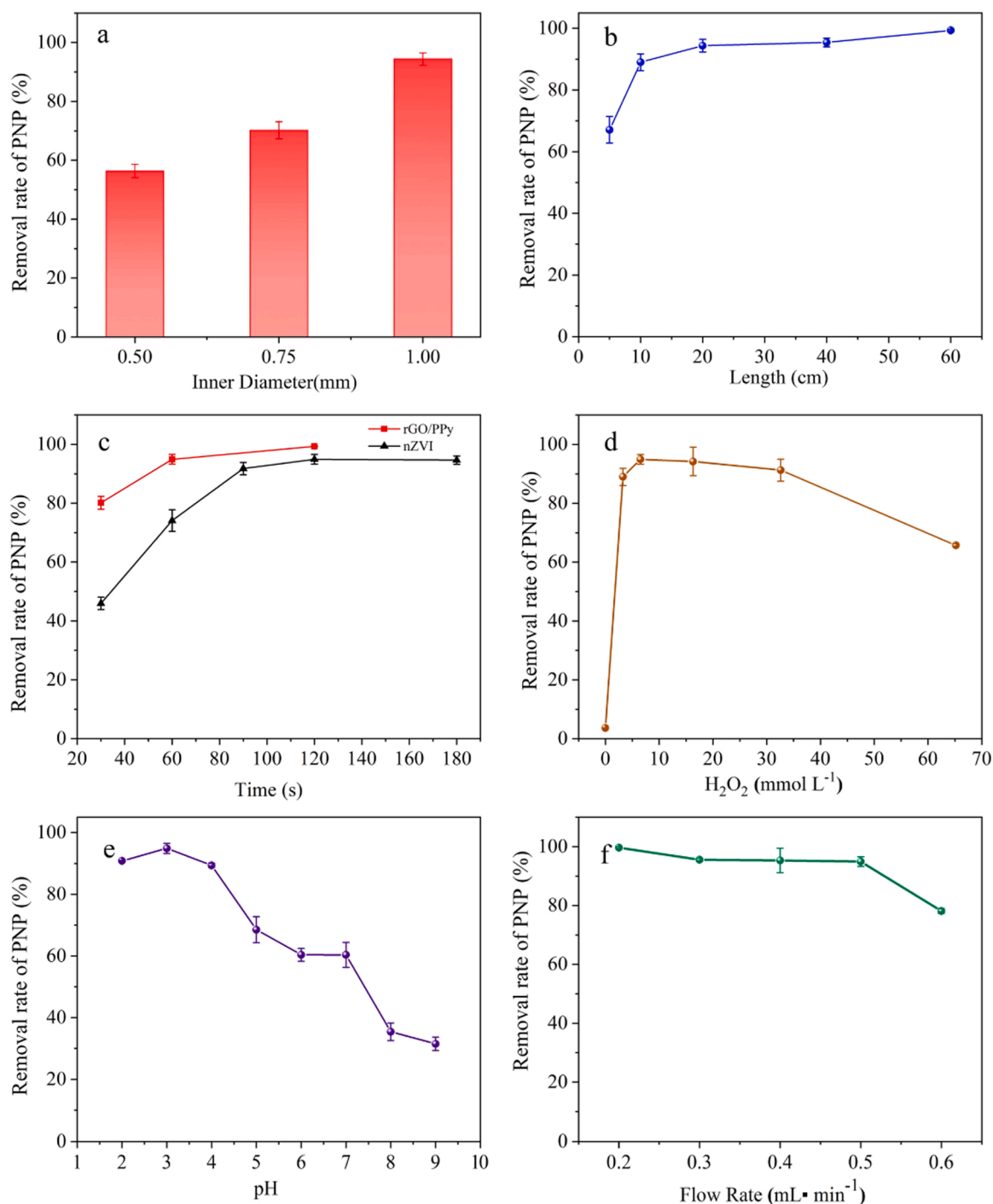
**Fig. 4.** Effect of (a) inner diameter, (b) length of microreactor, (c) electrodeposition time, (d) oxidant dosage, (e) pH and (f) flow rate on the removal of PNP by rGO/PPy/nZVI microreactor. The following conditions were used unless otherwise stated: [PNP]= 10 mg L$^{-1}$, flow rate= 0.5 mL min$^{-1}$, pH= 3, [H$_2$O$_2$]= 6.52 mmol/L.

(Fig. 4f). The results showed that both the adsorption and oxidation of PNP on rGO/PPy/nZVI membrane could be well achieved within τ of 20 s (0.5 mL min$^{-1}$), thanks to the fast convection-enhanced diffusion and mass transfer of the microreactor configuration. This was significantly advantageous over the conventional nZVI batch reactors, during which fast adsorption but much slower oxidation of pollutants were often reported [12].

The performance of the rGO/PPy/nZVI microreactor was further compared with the rGO/PPy, PPy/nZVI, and nZVI counterparts (Fig. S9). With the identical residence time of 50 s, the rGO/PPy microreactor only removed 8.3% PNP, much lower than the efficiency of

rGO/PPy/nZVI (99.6%), indicating that the PNP removal mainly resulted from the nZVI catalyzed Fenton-like degradation rather than the adsorption of rGO/PPy. Besides, the PNP removal efficiency in the PPy/nZVI and nZVI microreactors were less than 80%, indicating the indispensable role of the rGO/PPy composite substrate to support the high Fenton-like activity of nZVI. Moreover, the performance of the rGO/PPy/nZVI microreactor was further compared with several previous reports (Table S1) [5,47–51]. The rGO/PPy/nZVI microreactor outperformed these reports to achieve the ultrafast removal of PNP, demonstrating the advantages of our rGO/PPy/nZVI nanocomposite and the microreactor design. The total organic carbon (TOC) removal

efficiency by the rGO/PPy/nZVI microreactor was ca. 19% at the optimal parameters, and the relatively lower TOC removal performance than PNP removal was reasonable and acceptable since some degrading intermediates of PNP shall be less susceptible to Fenton-like oxidation.

### 3.3. Reusability and regeneration study

Reusability is an important criterion to evaluate catalyst performance because it can save costs in practical applications [52]. The recyclability of the rGO/PPy/nZVI microreactor was assessed by successive operations at the flow rate of 0.2 mL min$^{-1}$, and the PNP concentration in the effluent was monitored every 5 min. The PNP removal performance of the rGO/PPy/nZVI microreactor basically maintained within 5 cycles, and decreased to 48.5% at the 6th cycle. This showed significant improvement when compared with the recycling performance of the nZVI microreactor, which sharply decreased to 4.6% after 5 cycles (Fig. 5a). We then characterized the used rGO/PPy/nZVI and nZVI samples after different cycles with XPS analysis, in order to investigate the better durability of rGO/PPy/nZVI (Fig. S10). A notable increase of the Fe(III)/Fe(II) ratio from 2.7 to 4.31 after 6 successive cycles in the nZVI microreactor indicated the significant oxidization of nZVI during the Fenton-like reaction (Fig. 5b and Figs. S10i-S10l). Intriguingly, the Fe(III)/Fe(II) ratio of the rGO/PPy/nZVI microreactor did not increase obviously, suggesting that the Fe(III) probably underwent effective reduction to regenerate Fe(II) in the rGO/PPy/nZVI microreactor (Figs. 5b and S10e-h). The enhanced stability of rGO/PPy/nZVI might resulted from the synergistic interfacial effect between the rGO/PPy substrate and the nZVI. As displayed in XPS C1s spectra of rGO/PPy/nZVI, the proportion of C-C/C=C gradually decreased during the recycling experiments, along with the steady increase of C–O and C=O composites (Figs. 5c, and S10a-d). These results indicated that the rGO underwent oxidation during the reaction, and possibly donated the unpaired π electrons to reduce the Fe(III) to Fe(II) [30]. Therefore, the rGO/PPy substrate could simultaneously anchor the nZVI particles and promote the redox cycle of iron species, whereby alleviate the oxidation of nZVI and the deactivation of the rGO/PPy/nZVI microreactor [53].

Some inorganic anions in the environmental water matrices often have deleterious effects on the performance of AOPs [54]. Herein we investigated the impacts of several typical inorganic anions ($SO_4^{2-}$, $NO_3^-$, $HPO_4^{2-}$). $SO_4^{2-}$ had almost no effect on the removal of PNP, whereas $NO_3^-$ and $HPO_4^{2-}$ led to the decrease of PNP removal by 16.55% and 36.98%, respectively (Fig. 6a). $NO_3^-$ was reported to be directly reduced by nZVI, thus competed electrons with $H_2O_2$ and reduced the generation of reactive species [12,55]. $HPO_4^{2-}$ may form complex with $Fe^{2+}$ [47], or adsorb on the surface of nZVI to passivate it. Moreover, these anions could also quench the OH• to generate less reactive radicals [56]. The rGO/PPy/nZVI microreactor was also used to remove PNP from a real

environmental water matrix collected from East Lake, Wuhan, China. The initial PNP removal efficiency was 77.6% within 5 min, slightly lower than that in pure water due to the presence of complicated water matrices in environmental water samples including inorganic ions, natural organic matter, and microorganisms, which might scavenge the reactive species or block catalytic active sites. Satisfying removal of PNP could be maintained across a duration of 20 min, but relatively low removal ratios were observed beyond 20 min, similar with the case in pure water (Fig. 6b).

To investigate the mechanism of the attenuated catalytic performance, the rGO/PPy/nZVI membrane was examined by XRD and SEM analysis. As depicted in Fig. S11a, the XRD pattern of the used rGO/PPy/nZVI membrane did not show significant difference when compared with the fresh fabricated sample, except that the peak intensities at 2θ = 44.71°, 65.18° and 82.38°decreased slightly. Nevertheless, the SEM images (Fig. S11b and 11c) of the used rGO/PPy/nZVI presented that the dendritic structure of nZVI disappeared, and the catalyst surface was covered by many fibrous and wrinkled substance, attributed to the in-situ formed amorphous iron oxides during the Fenton-like reaction, which might lead to the deactivation of the catalyst. The iron dissolution in the effluent was also monitored, and the concentrations of total Fe ions were in the range of 8.1–13.0 mg L$^{-1}$. The slow release of iron would contribute to the degradation of PNP thanks to the homogeneous Fenton reaction, but may deteriorate the heterogeneous rGO/PPy/nZVI catalysis amid recycling. Nevertheless, the deactivated rGO/PPy/nZVI microreactor can be easily regenerated by HCl washing and re-electrodeposition of nZVI, to restore 96.7% PNP removal (Fig. S12). A scaled-up microreactor array was thus proposed as Fig. S13, which is expected to bring new opportunities for the actual wastewater treatment.

### 3.4. Possible mechanism of the rGO/PPy/nZVI Fenton-like reaction

DFT calculation was used to gain further insight into the formation of rGO/PPy supported nZVI catalyst. The calculation results in Fig. 7 suggested that PPy promoted the adsorption of Fe atom on rGO, since the length of Fe-C bond shortened from 2.257 and 2.259 Å on rGO (bridge site, Figs. 7c) to 2.168 Å on rGO/PPy (top site, Fig. 7a). Besides, the changes of Gibbs free energy (ΔG) and adsorption enthalpy (ΔH$_{ads}$) were − 0.150 and − 0.421 eV during the adsorption of Fe atom on rGO, which decreased to − 0.285 and − 0.565 eV in the presence of PPy. Therefore, the introduction of PPy facilitated the anchoring of nZVI on the surface of rGO, thus promoted the subsequent nucleation of iron, resulting in the increased nucleation sites and smaller size of nZVI.

The catalytic decomposition of $H_2O_2$ on the rGO/PPy/nZVI was also simulated by the DFT calculation. In the rGO/nZVI composite without PPy, the interaction between nZVI and rGO was weak (Fig. 7c), and
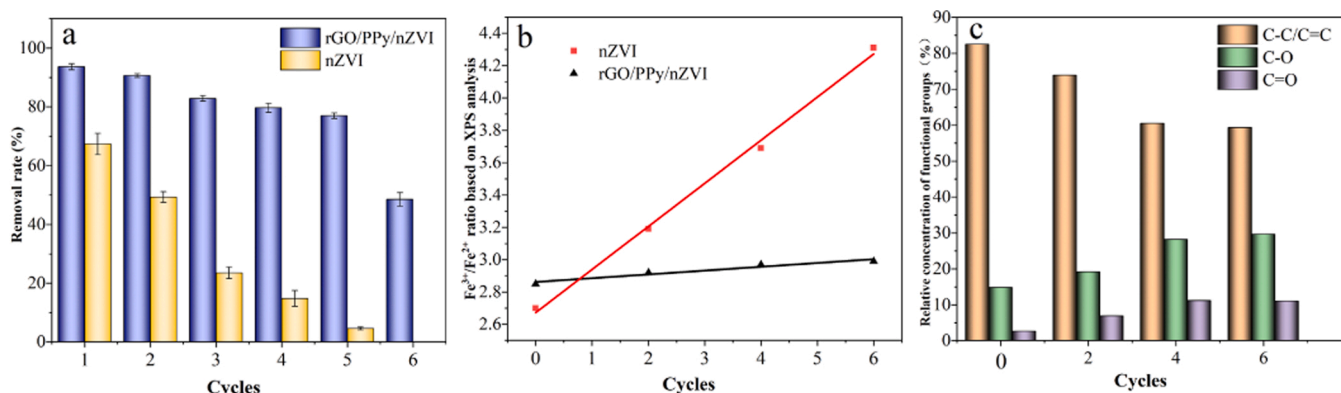


**Fig. 5.** (a) Long-term stability of rGO/PPy/nZVI and nZVI microreactor (per cycle conditions: flow rate: 0.2 mL min$^{-1}$, reaction time: 5 min, [PNP]: 10 mg L$^{-1}$), (b) Fe$^{3+}$/Fe$^{2+}$ ratio based on XPS analysis on rGO/PPy/nZVI catalyst, (c) relative concentration of functional groups on C 1 s spectra of rGO/PPy/nZVI microreactor based on XPS analysis.
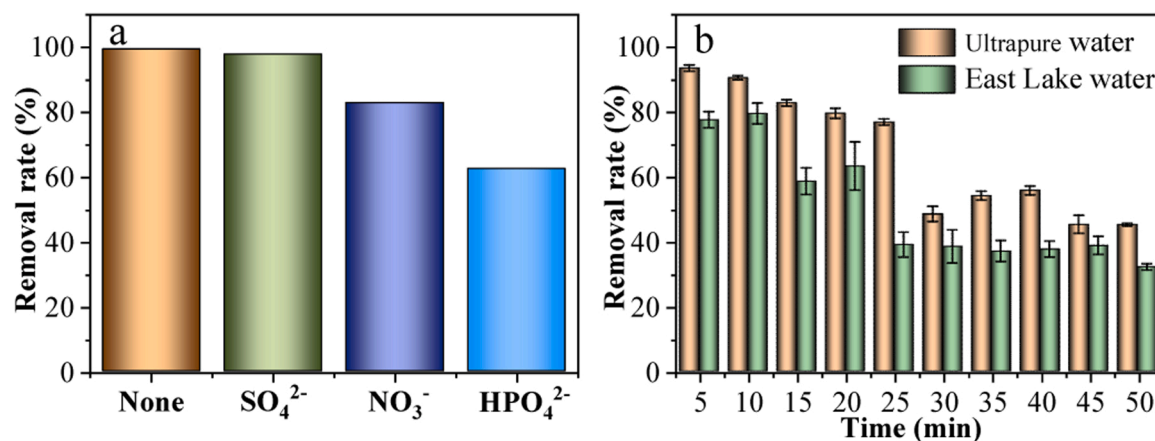
**Fig. 6.** (a) Effects of different inorganic anions (flow rate: 0.2 mL min$^{-1}$, [SO$_4^{2-}$]=10 mM, [NO$_3^-$]= 10 mM, [HPO$_4^{2-}$]= 10 mM, pH= 3, [PNP]= 10 mg L$^{-1}$, [H$_2$O$_2$]= 6.52 mM). (b) Catalytic performance of rGO/PPy/nZVI catalytic microreactor in ultrapure water and East Lake water for long-term running (flow rate: 0.2 mL min$^{-1}$, PNP initial concentration: 10 mg L$^{-1}$).
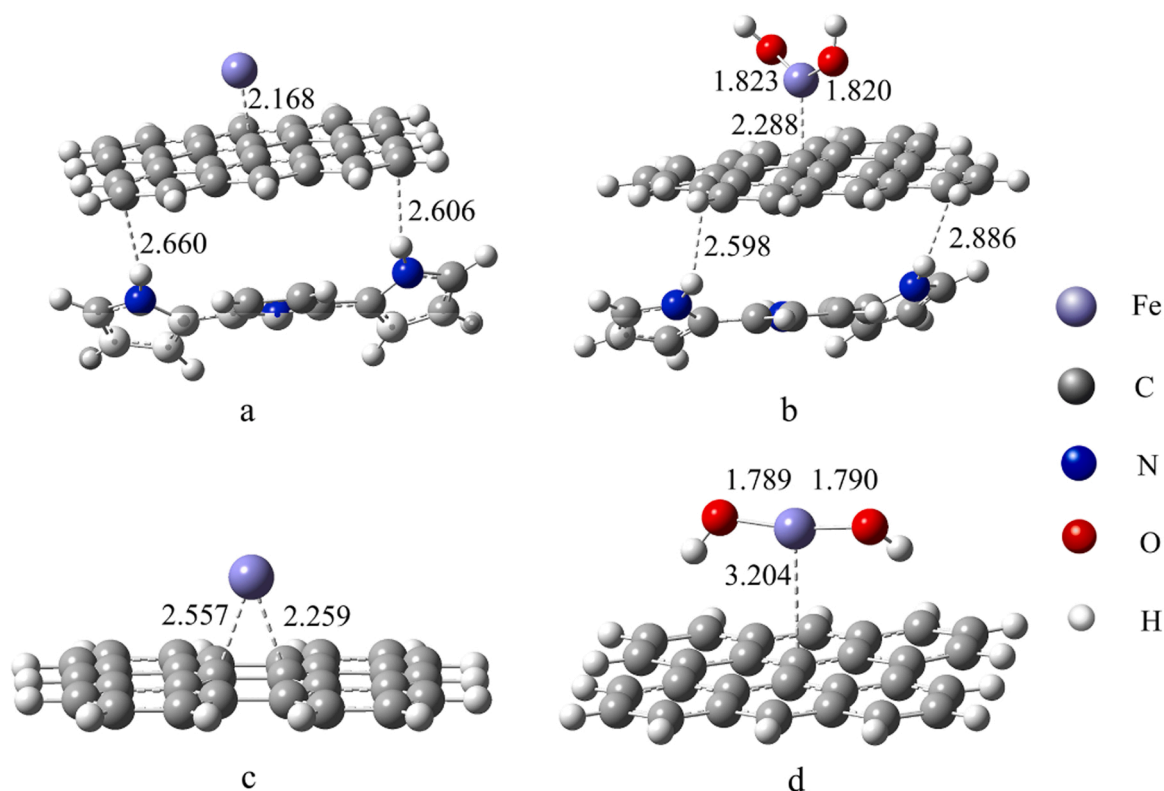


**Fig. 7.** DFT optimized geometries of (a) rGO/PPy/nZVI and (c) rGO/nZVI, as well as those of H$_2$O$_2$ adsorption on (b) rGO/PPy/nZVI and (d) rGO/nZVI.

when H$_2$O$_2$ was adsorbed on the Fe atom, the Fe-C bond was elongated significantly to 3.204 Å (Fig. 7d), further weakening the Fe-C interaction. However, in the rGO/PPy/nZVI composite, the Fe-C interacted more closely (Fig. 7a), and electron-transfer from Fe atom to rGO/PPy substrate (0.3279 e) was obtained. Besides, natural bond orbital (NBO) analysis showed the weak electron transfer from N-H bonding orbital of PPy to antibonding orbital π * (C-C) of rGO (0.0248 e) (Fig. S14). These results indicated that the presence of PPy is favorable for the formation of more stable electron-transfer complex between nZVI, rGO and PPy, which may facilitate the subsequent decomposition of H$_2$O$_2$ to •OH. However, no stable adsorption complex between H$_2$O$_2$ and the rGO/PPy/nZVI was found, because the Fe atom immediately inserted into the O-O bond of H$_2$O$_2$ once H$_2$O$_2$ was adsorbed, leading to the homolytic

cleavage of O-O bond to adsorbed •OH, with the length of Fe-OH bond of 1.820–1.823 Å (Fig. 7b), significantly longer than those (1.789 and 1.790 Å) in the rGO/nZVI-H$_2$O$_2$ system (Fig. 7d). The longer Fe-OH bond is beneficial for the generation of free •OH and the recovery of Fe active sites, therefore, the rGO/PPy/nZVI composite would exhibit better performance in the Fenton-like reaction. In addition, strong electron transfer was observed from both C-C bonding orbital of PPy and antibonding orbital π * (C-C) of rGO to unoccupied orbital of Fe(III) (Fig. S15), resulting in the reduction of Fe(III) to regenerate Fe(II), suggested that the synergistic interaction between rGO/PPy and nZVI could accelerate the Fe(III)/Fe(II) redox cycle and the subsequent Fenton reaction.

To gain more insights into the mechanism of the rGO/PPy/nZVI

Fenton-like reaction, the reactive species were clarified. Radical scavenging experiments were conducted with isopropanol (IPA) and chloroform (CF) as the scavengers of •OH and $O_2^{•-}$. According to Fig. S16, PNP degradation efficiency decreased to 40% and 29% in the presence of 100 mM CF and 100 mM IPA, respectively, suggesting that both $O_2^{•-}$ and •OH radicals were responsible reactive species (Fig. S16a). To confirm the role of $O_2^{•-}$, we further employed 1,4-benzoquinone (PBQ) and superoxide dismutase (SOD) as scavengers, which showed similar inhibition of PNP removal with CF. Besides, the inhibition of PNP removal by both IPA and CF clearly showed the dose dependent manner. Higher concentrations of scavengers suppressed the removal of PNP more significantly, thanks to the stronger competitive consumption of •OH and $O_2^{•-}$ by IPA and CF at higher concentrations (Fig. S16b and c). These results confirmed the contribution of •OH and $O_2^{•-}$ to PNP degradation in the rGO/PPy/nZVI-$H_2O_2$ Fenton-like reaction. The production of •OH and $O_2^{•-}$ was also monitored by the spin trap technique in electron paramagnetic resonance (EPR) spectroscopy. The quadruple peak signals of DMPO-•OH adduct (1:2:2:1) were observed in the rGO/PPy/nZVI-$H_2O_2$ reaction (Fig. S17a), confirming the production of •OH [57]. Moreover, when methanol was used as the solvent to scavenge •OH, the typical EPR signals of the DMPO-superoxide radical adduct was observed (Fig. S17b), demonstrating the generation of $O_2^{•-}$.

To further investigate the pathways of PNP degradation in the rGO/PPy/nZVI microreactor, LC-MS analysis was conducted to identify the organic course products. Maleic acid, fumaric acid, pyruvic acid, oxalic acid, acetic acid and formic acid were found in the eluent of microreactor, with their mass spectra and chromatograms shown in Fig. S18 and Table S2. The possible pathways of PNP degradation were proposed (Scheme 1). The nitro- group of PNP was replaced by •OH attack to generate hydroquinone[46], which was then rapidly oxidized to *p*-benzoquinone (PBQ) due to orientation of substituents [58]. The $O_2^{•-}$ was proposed to reduce the nitro- group of PNP, producing 4-aminophenol [59]. However, we did not detect hydroquinone, PBQ and 4-aminophenol, possibly due to their high susceptibility toward subsequent •OH oxidation [47]. •OH attack further opened the benzene rings of intermediates and yielded small molecular organic acids such as maleic acid, fumaric acid, pyruvic acid, acetic acid, oxalic acid, and formic acid [60]. Further mineralization of these intermediates to $CO_2$ and $H_2O$ was finally expected.

Based on the above results, a possible mechanism of the PNP removal by the rGO/PPy/nZVI-$H_2O_2$ heterogeneous Fenton-like reaction is proposed (Scheme 2). First, $H_2O_2$ and PNP were adsorbed on the surface of the rGO/PPy/nZVI composite due to the two-dimensional layered structure and ultrahigh surface area of rGO which resulted in the π-π and p-π conjugation interaction between PNP and rGO. The presence of PPy promoted the anchoring of nZVI on the rGO/PPy substrate to form the stable rGO/PPy/nZVI nanocomposite. nZVI can react with $H^+$ and $H_2O_2$ to produce surface confined iron species ($\equiv Fe^{II}$ and $\equiv Fe^{III}$), which then activated $H_2O_2$ to produce •OH and $O_2^{•-}$ for the degradation of the adjacently adsorbed PNP. Besides, the $O_2^{•-}$ could initiate the redox cycle of $\equiv Fe^{III}/\equiv Fe^{II}$ for better Fenton-like reactions. In addition, excellent electron conductivity of rGO and PPy can promote the electron transfer between nZVI and the rGO/PPy substrate, thus enhanced the catalytic performance [28]. The $\equiv Fe^{II}$ would also dissolve ($Fe^{2+}$) and catalyze the homogeneous Fenton reaction, leading to the rapid degradation of PNP [61]. In addition, the $\equiv Fe^{III}/Fe^{3+}$ can be reduced by nZVI and rGO/PPy to regenerate $\equiv Fe^{II}/Fe^{2+}$, improving the efficiency of Fenton-like reactions. On the other hand, the continuous flow-by mode of reaction could remove the degraded byproducts of PNP from the rGO/PPy/nZVI catalysts promptly, thus endowed the microreactor with a timely refreshed catalyst surface and ultrahigh catalytic performance.

## 4. Conclusions

In summary, a novel rGO/PPy/nZVI catalytic microreactor was successfully constructed by a facile two-step electrodeposition method, with nZVI evenly dispersed and immobilized on the rGO/PPy supporting membrane. High p-nitrophenol (PNP) removal rate of > 99% can be obtained in 50 s, and relatively good reusability was obtained. The high performance of rGO/PPy/nZVI microreactor was due to the well dispersion of nZVI, the synergistic effects between rGO/PPy composite substrate and nZVI for the solid anchor of nZVI, the effective activation of $H_2O_2$, and the better redox cycle of Fe(III)/Fe(II). The results of the study are expected to bring about new opportunities in the development of efficient microreactor arrays for the water treatment industry.

## CRediT authorship contribution statement

**Yanyan Chen:** Investigation, Visualization, Writing – original draft. **Manlin Zhang:** Investigation. **Tiantian Chen:** Validation. **Ganbing Zhang:** Investigation. **Hui Xu:** Methodology, Supervision, Writing – review & editing, Funding acquisition. **Hongwei Sun:** Methodology, Writing – review & editing, Funding acquisition. **Lizhi Zhang:** Writing – review & editing, Supervision.
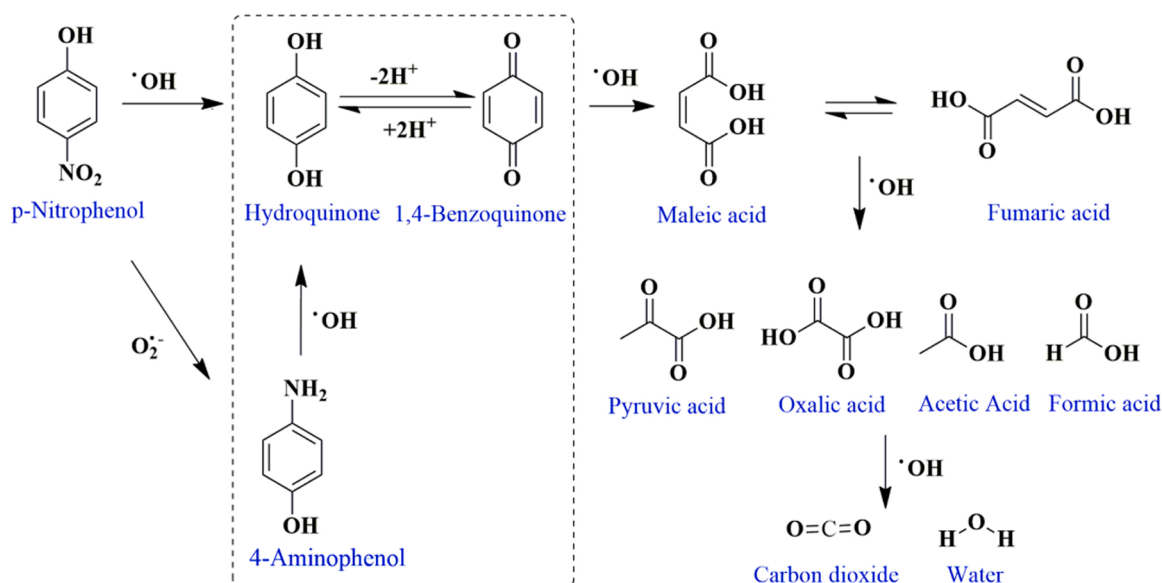


**Scheme 1.** Possible degradation pathways of PNP in the rGO/PPy/nZVI microreactor.
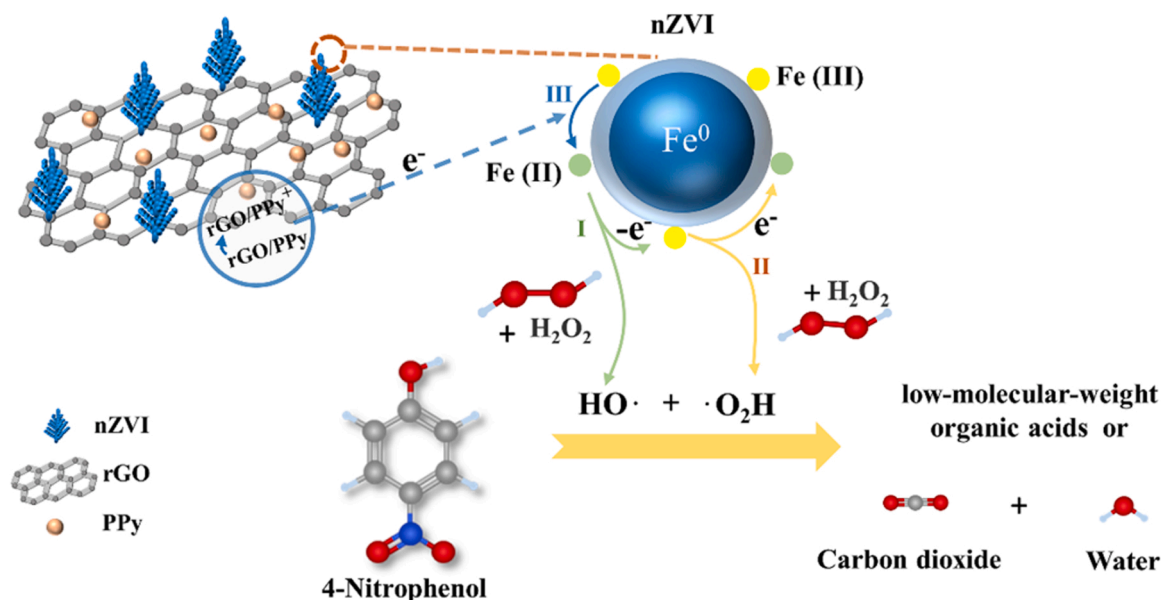
**Scheme 2.** Possible mechanism of the rGO/PPy/nZVI microreactor catalyzed Fenton-like reaction to remove PNP.

## Declaration of Competing Interest

The authors declare that they have no known competing financial interests or personal relationships that could have appeared to influence the work reported in this paper.

## Data availability

Data will be made available on request.

## Acknowledgments

## Appendix A. Supporting information

Supplementary data associated with this article can be found in the online version at doi:10.1016/j.apcatb.2022.122270.

## References

[1] L. Yao, H. Yang, Z. Chen, M. Qiu, B. Hu, X. Wang, Bismuth oxychloride-based materials for the removal of organic pollutants in wastewater, Chemosphere 273 (2021), 128576, https://doi.org/10.1016/j.chemosphere.2020.128576.
[2] M. Hao, M. Qiu, H. Yang, B. Hu, X. Wang, Recent advances on preparation and environmental applications of MOF-derived carbons in catalysis, Sci. Total Environ. 760 (2021), 143333, https://doi.org/10.1016/j.scitotenv.2020.143333.
[3] M. Fang, X. Tan, Z. Liu, B. Hu, X. Wang, Recent progress on metal-enhanced photocatalysis: a review on the mechanism, Research 2021 (2021), 9794329, https://doi.org/10.34133/2021/9794329.
[4] K. Akbar, E. Moretti, A. Vomiero, Carbon dots for photocatalytic degradation of aqueous pollutants: recent advancements, Adv. Opt. Mater. 9 (2021), 2100532, https://doi.org/10.1002/adom.202100532.
[5] J. Li, Q. Ji, B. Lai, D. Yuan, Degradation of p-nitrophenol by Fe⁰/H₂O₂/persulfate system: optimization, performance and mechanisms, J. Taiwan Inst. Chem. E 80 (2017) 686–694, https://doi.org/10.1016/j.jtice.2017.09.002.
[6] W. Wang, P. Zhao, Y. Hu, R. Zan, Application of weak magnetic field coupling with zero-valent iron for remediation of groundwater and wastewater: a review, J. Clean. Prod. 262 (2020), 121341, https://doi.org/10.1016/j.jclepro.2020.121341.
[7] M. Stefaniuk, P. Oleszczuk, Y.S. Ok, Review on nano zerovalent iron (nZVI): From synthesis to environmental applications, Chem. Eng. J. 287 (2016) 618–632, https://doi.org/10.1016/j.cej.2015.11.046.
[8] A.N. Garcia, Y. Zhang, S. Ghoshal, F. He, D.M. O'Carroll, Recent advances in sulfidated zerovalent iron for contaminant transformation, Environ. Sci. Technol. 55 (2021) 8464–8483, https://doi.org/10.1021/acs.est.1c01251.
[9] S. Li, W. Wang, F. Liang, W. Zhang, Heavy metal removal using nanoscale zero-valent iron (nZVI): Theory and application, J. Hazard. Mater. 322 (2017) 163–171, https://doi.org/10.1016/j.jhazmat.2016.01.032.
[10] A.S. Ruhl, C. Kotré, U. Gernert, M. Jekel, Identification, quantification and localization of secondary minerals in mixed Fe⁰ fixed bed reactors, Chem. Eng. J. 172 (2011) 811–816, https://doi.org/10.1016/j.cej.2011.06.067.
[11] C. Xu, X. Pan, L. Fang, J. Li, F. Li, Enhanced reduction of organic pollutants by Fe/Cu@Pd ternary metallic nanoparticles under aerobic conditions: Batch and membrane reactor studies, Chem. Eng. J. 360 (2019) 180–189, https://doi.org/10.1016/j.cej.2018.11.212.
[12] R. Xing, J. He, P. Hao, W. Zhou, Graphene oxide-supported nanoscale zero-valent iron composites for the removal of atrazine from aqueous solution, Colloids Surf. A Physicochem. Eng. Asp. 589 (2020), 124466, https://doi.org/10.1016/j.colsurfa.2020.124466.
[13] M. Raji, S.A. Mirbagheri, F. Ye, J. Dutta, Nano zero-valent iron on activated carbon cloth support as fenton-like catalyst for efficient color and COD removal from melanoidin wastewater, Chemosphere 263 (2021), 127945, https://doi.org/10.1016/j.chemosphere.2020.127945.
[14] X. Ling, J. Li, W. Zhu, Y. Zhu, X. Sun, J. Shen, W. Han, L. Wang, Synthesis of nanoscale zero-valent iron/ordered mesoporous carbon for adsorption and synergistic reduction of nitrobenzene, Chemosphere 87 (2012) 655–660, https://doi.org/10.1016/j.chemosphere.2012.02.002.
[15] Z. Chen, D. Wei, Q. Li, X. Wang, S. Yu, L. Liu, B. Liu, S. Xie, J. Wang, D. Chen, T. Hayat, X. Wang, Macroscopic and microscopic investigation of Cr(VI) immobilization by nanoscaled zero-valent iron supported zeolite MCM-41 via batch, visual, XPS and EXAFS techniques, J. Clean. Prod. 181 (2018) 745–752, https://doi.org/10.1016/j.jclepro.2018.01.231.
[16] L. Yang, L. Chen, D. Ouyang, J. Yan, L. Qian, L. Han, M. Chen, J. Li, M. Gu, Mechanistic insights into adsorptive and oxidative removal of monochlorobenzene in biochar-supported nanoscale zero-valent iron/persulfate system, Chem. Eng. J. 400 (2020), 125811, https://doi.org/10.1016/j.cej.2020.125811.
[17] D. Shi, G. Zhu, X. Zhang, M. Cheng, T. Wu, K. Zhang, J. Fan, Decorating of ultra small and recyclable nanoscale zero-valent iron on NH₂-SiO₂ for enhanced high-performance removal of water pollutants, J. Alloy. Compd. 782 (2019) 183–192, https://doi.org/10.1016/j.jallcom.2018.12.128.
[18] R. Munirathinam, J. Huskens, W. Verboom, Supported catalysis in continuous-flow microreactors, Adv. Synth. Catal. 357 (2015) 1093–1123, https://doi.org/10.1002/adsc.201401081.
[19] K. Jähnisch, V. Hessel, H. Löwe, M. Baerns, Chemistry in microstructured reactors, Angew. Chem. Int. Ed. 43 (2004) 406–446, https://doi.org/10.1002/anie.200300577.
[20] M. Guidotti, N. Ravasio, R. Psaro, E. Gianotti, S. Coluccia, L. Marchese, Epoxidation of unsaturated FAMEs obtained from vegetable source over Ti(IV)-grafted silica catalysts: a comparison between ordered and non-ordered mesoporous materials, J. Mol. Catal. A Chem. 250 (2006) 218–225, https://doi.org/10.1016/j.molcata.2006.01.032.
[21] S. Phimsen, H. Yamada, T. Tagawa, W. Kiatkittipong, K. Kiatkittipong, N. Laosiripojana, S. Assabumrungrat, Epoxidation of methyl oleate in a TiO₂

coated-wall capillary microreactor, Chem. Eng. J. 314 (2017) 594–599, https://doi.org/10.1016/j.cej.2016.12.017.

[22] Y. Liu, X. Liu, S. Yang, F. Li, C. Shen, M. Huang, J. Li, R.R. Nasaruddin, J. Xie, Rational design of high-performance continuous-flow microreactors based on gold nanoclusters and graphene for catalysis, ACS Sustain. Chem. Eng. 6 (2018) 15425–15433, https://doi.org/10.1021/acssuschemeng.8b03858.

[23] Y. Chen, G. Zhang, H. Liu, J. Qu, Confining free radicals in close vicinity to contaminants enables ultrafast fenton-like processes in the interspacing of MoS₂ membranes, Angew. Chem. Int. Ed. 58 (2019) 8134–8138, https://doi.org/10.1002/anie.201903531.

[24] L. Zhang, X. Yang, E. Han, L. Zhao, J. Lian, Reduced graphene oxide wrapped Fe₃O₄-Co₃O₄ yolk-shell nanostructures for advanced catalytic oxidation based on sulfate radicals, Appl. Surf. Sci. 396 (2017) 945–954, https://doi.org/10.1016/j.apsusc.2016.11.066.

[25] K. Gopalakrishnan, S. Sultan, A. Govindaraj, C.N.R. Rao, Supercapacitors based on composites of PANI with nanosheets of nitrogen-doped RGO, BC₁.₅N, MoS₂ and WS₂, Nano Energy 12 (2015) 52–58, https://doi.org/10.1016/j.nanoen.2014.12.005.

[26] C.C. Li, H. Yu, Q. Yan, H.H. Hng, Green synthesis of highly reduced graphene oxide by compressed hydrogen gas towards energy storage devices, J. Power Sources 274 (2015) 310–317, https://doi.org/10.1016/j.jpowsour.2014.10.056.

[27] X. Yang, P. Pachfule, Y. Chen, N. Tsumori, Q. Xu, Highly efficient hydrogen generation from formic acid using a reduced graphene oxide-supported AuPd nanoparticle catalyst, Chem. Commun. 52 (2016) 4171–4174, https://doi.org/10.1039/c5cc10311h.

[28] T. Yuan, Y. Jiang, W. Sun, B. Xiang, Y. Li, M. Yan, B. Xu, S. Dou, Ever-increasing pseudocapacitance in RGO-MnO-RGO sandwich nanostructures for ultrahigh-rate lithium storage, Adv. Funct. Mater. 26 (2016) 2198–2206, https://doi.org/10.1002/adfm.201504849.

[29] M. Gu, Q. Sui, U. Farooq, X. Zhang, Z. Qiu, S. Lyu, Degradation of phenanthrene in sulfate radical based oxidative environment by nZVI-PDA functionalized rGO catalyst, Chem. Eng. J. 354 (2018) 541–552, https://doi.org/10.1016/j.cej.2018.08.039.

[30] N.A. Zubir, C. Yacou, J. Motuzas, X. Zhang, X.S. Zhao, J.C. Diniz da Costa, The sacrificial role of graphene oxide in stabilising a fenton-like catalyst GO-Fe₃O₄, Chem. Commun. 51 (2015) 9291–9293, https://doi.org/10.1039/c5cc02292d.

[31] D. Chen, H. Xu, Simultaneous HPLC-MS determination of 8-hydroxy-2'-deoxyguanosine, 3-hydroxyphenanthrene and 1-hydroxypyrene after online in-tube solid phase microextraction using a graphene oxide/poly(3,4-ethylenedioxythiophene)/polypyrrole composite, Mikrochim. Acta 186 (2019) 300, https://doi.org/10.1007/s00604-019-3429-2.

[32] A.I. Pruna, N.M. Rosas-Laverde, D. Busquets Mataix, Effect of deposition parameters on electrochemical properties of polypyrrole-graphene oxide films, Materials 13 (2020) 624, https://doi.org/10.3390/ma13030624.

[33] Y.S. Lim, Y.P. Tan, H.N. Lim, W.T. Tan, M.A. Mahnaz, Z.A. Talib, N.M. Huang, A. Kassim, M.A. Yarmo, Polypyrrole/graphene composite films synthesized via potentiostatic deposition, J. Appl. Polym. Sci. 128 (2013) 224–229, https://doi.org/10.1002/app.38174.

[34] Z. Yu, Z. Yao, N. Zhang, Z. Wang, C. Li, X. Han, X. Wu, Z. Jiang, Electric field-induced synthesis of dendritic nanostructured α-Fe for electromagnetic absorption application, J. Mater. Chem. A. 1 (2013) 4571–4576, https://doi.org/10.1039/c3ta01641b.

[35] U. Farooq, J. Zhuang, X. Wang, S. Lyu, A recyclable polydopamine-functionalized reduced graphene oxide/Fe nanocomposite (PDA@Fe/rGO) for the enhanced degradation of 1,1,1-trichloroethane, Chem. Eng. J. 403 (2021), 126405, https://doi.org/10.1016/j.cej.2020.126405.

[36] J. Li, C. Chen, R. Zhang, X. Wang, Reductive immobilization of Re(VII) by graphene modified nanoscale zero-valent iron particles using a plasma technique, Sci. China Chem. 59 (2016) 150–158, https://doi.org/10.1007/s11426-015-5452-4.

[37] C. Wang, H. Luo, Z. Zhang, Y. Wu, J. Zhang, S. Chen, Removal of As(III) and As(V) from aqueous solutions using nanoscale zero valent iron-reduced graphite oxide modified composites, J. Hazard. Mater. 268 (2014) 124–131, https://doi.org/10.1016/j.jhazmat.2014.01.009.

[38] Z.S. Wu, W. Ren, L. Gao, B. Liu, C. Jiang, H.M. Cheng, Synthesis of high-quality graphene with a pre-determined number of layers, Carbon 47 (2009) 493–499, https://doi.org/10.1016/j.carbon.2008.10.031.

[39] X.Y. Peng, X.X. Liu, D. Diamond, K.T. Lau, Synthesis of electrochemically-reduced graphene oxide film with controllable size and thickness and its use in supercapacitor, Carbon 49 (2011) 3488–3496, https://doi.org/10.1016/j.carbon.2011.04.047.

[40] S. Boursiquot, M. Mullet, J.-J. Ehrhardt, XPS study of the reaction of chromium (VI) with mackinawite (FeS), Surf. Interface Anal. 34 (2002) 293–297, https://doi.org/10.1002/sia.1303.

[41] L. Xu, J. Wang, Magnetic nanoscaled Fe₃O₄/CeO₂ composite as an efficient fenton-like heterogeneous catalyst for degradation of 4-chlorophenol, Environ. Sci. Technol. 46 (2012) 10145–10153, https://doi.org/10.1021/es300303f.

[42] W. Yan, A.A. Herzing, X.Q. Li, C.J. Kiely, W.X. Zhang, Structural evolution of Pd-doped nanoscale zero-valent iron (nZVI) in aqueous media and implications for particle aging and reactivity, Environ. Sci. Technol. 44 (2010) 4288–4294, https://doi.org/10.1021/es100051q.

[43] M. Dickinson, T.B. Scott, The application of zero-valent iron nanoparticles for the remediation of a uranium-contaminated waste effluent, J. Hazard. Mater. 178 (2010) 171–179, https://doi.org/10.1016/j.jhazmat.2010.01.060.

[44] J. Cao, X. Li, J. Tavakoli, W.X. Zhang, Temperature programmed reduction for measurement of oxygen content in nanoscale zero-valent iron, Environ. Sci. Technol. 42 (2008) 3780–3785, https://doi.org/10.1021/es7027845.

[45] Q. Xia, Z. Jiang, J. Wang, Z. Yao, A facile preparation of hierarchical dendritic zero-valent iron for fenton-like degradation of phenol, Catal. Commun. 100 (2017) 57–61, https://doi.org/10.1016/j.catcom.2017.06.017.

[46] Y. Guo, Q. Xue, H. Zhang, N. Wang, S. Chang, H. Wang, H. Pang, H. Chen, Treatment of real benzene dye intermediates wastewater by the fenton method: characteristics and multi-response optimization, RSC Adv. 8 (2018) 80–90, https://doi.org/10.1039/c7ra09404c.

[47] J. Du, Y. Wang, F. Faheem, T. Xu, H. Zheng, J. Bao, Synergistic degradation of PNP via coupling H₂O₂ with persulfate catalyzed by nano zero valent iron, RSC Adv. 9 (2019) 20323–20331, https://doi.org/10.1039/c9ra02901j.

[48] Y. Tian, M. Zhou, Y. Pan, J. Cai, G. Ren, Pre-magnetized Fe(0) as heterogeneous electro-fenton catalyst for the degradation of p-nitrophenol at neutral pH, Chemosphere 240 (2020), 124962, https://doi.org/10.1016/j.chemosphere.2019.124962.

[49] M. Liu, Z. Jia, P. Li, Y. Liu, M. Zhao, Y. Yang, Q. Huang, C. Yu, High Catalytic Activity of Fe₃₋ₓCuₓO₄/graphene oxide (0 ≤ x ≤ 0.1) nanocomposites as heterogeneous fenton catalysts for p-nitrophenol degradation, Water Air Soil Pollut. 230 (2019) 64, https://doi.org/10.1007/s11270-019-4121-1.

[50] L. Zeng, J. Gong, J. Dan, S. Li, J. Zhang, W. Pu, C. Yang, Novel visible light enhanced pyrite-fenton system toward ultrarapid oxidation of p-nitrophenol: catalytic activity, characterization and mechanism, Chemosphere 228 (2019) 232–240, https://doi.org/10.1016/j.chemosphere.2019.04.103.

[51] H. Luo, Y. Zhao, D. He, Q. Ji, Y. Cheng, D. Zhang, X. Pan, Hydroxylamine-facilitated degradation of rhodamine B (RhB) and p-nitrophenol (PNP) as catalyzed by Fe@Fe₂O₃ core-shell nanowires, J. Mol. Liq. 282 (2019) 13–22, https://doi.org/10.1016/j.molliq.2019.02.136.

[52] H. Sun, C. Liu, Y. Yao, Degradation of azo dyes using natural pyrite as fenton-like reaction catalyst, Environ. Eng. Sci. 38 (2021) 854–866, https://doi.org/10.1089/ees.2020.0359.

[53] A.R.D. Ahmad, S.S. Imam, W.D. Oh, R. Adnan, Fenton degradation of ofloxacin using a montmorillonite-Fe₃O₄ composite, Catalysts 11 (2021) 177, https://doi.org/10.3390/catal11020177.

[54] H. Dong, Q. Ning, L. Li, Y. Wang, B. Wang, L. Zhang, R. Tian, R. Li, J. Chen, Q. Xie, A comparative study on activation of persulfate by bare and surface-stabilized nanoscale zero-valent iron for the removal of sulfamethazine, Sep. Purif. Technol. 230 (2020), 115869, https://doi.org/10.1016/j.seppur.2019.115869.

[55] H. Zhou, S. Wu, Y. Zhou, Y. Yang, J. Zhang, L. Luo, X. Duan, S. Wang, L. Wang, D.C. W. Tsang, Insights into the oxidation of organic contaminants by iron nanoparticles encapsulated within boron and nitrogen co-doped carbon nanoshell: catalyzed fenton-like reaction at natural pH, Environ. Int. 128 (2019) 77–88, https://doi.org/10.1016/j.envint.2019.04.006.

[56] J. Cao, L. Lai, B. Lai, G. Yao, X. Chen, L. Song, Degradation of tetracycline by peroxymonosulfate activated with zero-valent iron: Performance, intermediates, toxicity and mechanism, Chem. Eng. J. 364 (2019) 45–56, https://doi.org/10.1016/j.cej.2019.01.113.

[57] W. Zhang, E. Fernandez-Fueyo, Y. Ni, M. van Schie, J. Gacs, R. Renirie, R. Wever, F. G. Mutti, D. Rother, M. Alcalde, F. Hollmann, Selective aerobic oxidation reactions using a combination of photocatalytic water oxidation and enzymatic oxyfunctionalisations, Nat. Catal. 1 (2018) 55–62, https://doi.org/10.1038/s41929-017-0001-5.

[58] M.A. Oturan, J. Peiroten, P. Chartrin, A.J. Acher, Complete destruction of p-nitrophenol in aqueous medium by electro-fenton method, Environ. Sci. Technol. 34 (2000) 3474–3479, https://doi.org/10.1021/es990901b.

[59] C. Zhang, T. Li, J. Zhang, S. Yan, C. Qin, Degradation of p-nitrophenol using a ferrous-tripolyphosphate complex in the presence of oxygen: the key role of superoxide radicals, Appl. Catal. B Environ. 259 (2019) 118030, https://doi.org/10.1016/j.apcatb.2019.118030.

[60] J. Meijide, E. Rosales, M. Pazos, M.A. Sanroman, p-nitrophenol degradation by electro-fenton process: pathway, kinetic model and optimization using central composite design, Chemosphere 185 (2017) 726–736, https://doi.org/10.1016/j.chemosphere.2017.07.067.

[61] H. Yao, S. Hu, Y. Wu, L. Fan, The synergetic effects in a fenton-like system catalyzed by nano zero-valent iron (nZVI), Pol. J. Environ. Stud. 28 (2019) 2491–2499, https://doi.org/10.15244/pjoes/91939.